Soft Matter

PAPER

View Article Online
View Journal

Cite this: DOI: 10.1039/d6sm00286b

The cocktail method: influence of microbubble shell homogeneity on acoustic behavior and stability

Pascal Poc,[a] Giulia Guerriero,[b] Johannes Büchler,[a] Tim Grossrieder,[a] Marco Cattaneo,[b] Gonzalo Collado-Lara,[b] Nathan Blanken,[a] Ines Oberhuber,[a] Justine Kusch,[c] Outi Supponen[b] and Simone Schuerle*[a]

The influence of lipid shell organization on the acoustic behavior of microbubbles (MBs) has become a focal point of ultrasound research. Recent studies have demonstrated that even monodisperse MBs from the same batch can exhibit profoundly different acoustic responses. As high-resolution ultrasound imaging and MB-assisted drug delivery continue to advance, this heterogeneity may compromise performance, causing artifacts and reducing localization accuracy. This study investigates phospholipid organization on the MB surface during both formation and dynamic volumetric changes. Using a panel of membrane probes and labeled lipids in combination with high-resolution confocal microscopy, we characterize lipid surface dynamics, phase behavior, and micro-viscosity. We introduce the 'cocktail method', a straightforward thermal procedure designed to produce seemingly domainless MBs and evaluate how these structural modifications influence acoustic behavior. Our results identify distinct characteristics among individual lipid components during shell formation and provide a qualitative assessment of viscosity within specific lipid phases during expansion and compression. Collectively, these findings reveal that lipid organization impacts shell elasticity and acoustic behavior. Furthermore, we show that the intrinsic physicochemical properties of the lipids DSPC and DSPE-PEG5000 drive an inevitable degree of phase separation that persists despite thermal quenching. This study aims to improve our understanding of the relationship between microbubble lipid architecture and its impact on shell viscoelasticity, stability, and acoustic behavior, ultimately aiding the development of predictable microbubbles for advanced medical applications.

Received 1st April 2026,
Accepted 2nd June 2026

DOI: 10.1039/d6sm00286b

rsc.li/soft-matter-journal

1. Introduction

Lipid-shelled MBs serve as contrast agents for contrast-enhanced ultrasound (CEUS) imaging.[1] By strongly scattering acoustic waves, MBs enhance image contrast and improve the visualization of vascular architecture and tissue perfusion. With the introduction of CEUS and the continuous development of advanced ultrasound imaging techniques like ultrasound localization microscopy (ULM),[2,3] ultrasound imaging has substantially refined spatial resolution and diagnostic accuracy.[4]

The key feature enabling CEUS is the unique acoustic response of MBs. When exposed to an ultrasound field, MBs undergo volumetric oscillations in response to a pressure wave. At specific excitation frequencies, typically near their resonance frequency, these oscillations become strongly nonlinear. As a result, MBs generate harmonic and subharmonic signals that are distinct from the predominantly linear backscatter of surrounding biological tissues. This nonlinear signature allows for the selective detection of MB signals and the effective suppression of tissue background, thereby enhancing image contrast.[5–7] Beyond their diagnostic utility, MBs have emerged as potent tools for improved drug delivery. Upon stimulation, MBs exert mechanical forces, including oscillatory 'push–pull' dynamics, microstreaming and cyclic jetting, which drive small molecules into cells and across biological barriers *via* sonoporation.[8,9]

Several interrelated parameters govern the acoustic behavior of MBs. While MB size is considered the primary determinant of resonance frequency and scattering efficiency,

[a] *Institute of Robotics and Intelligent Systems, Department of Health Sciences and Technology, ETH Zurich, Gloriastrasse 37/39, 8092 Zurich, Switzerland. E-mail: simone.schuerle@hest.ethz.ch*
[b] *Institute of Fluid Dynamics, Department of Mechanical and Process Engineering, ETH Zürich, Sonneggstrasse 3, 8092 Zürich, Switzerland*
[c] *ScopeM, Scientific Center of Optical and Electron Microscopy, ETH Zurich, Otto-Stern-Weg 3, 8093 Zürich, Switzerland*

the viscoelastic properties of the lipid shell also play a critical role.[10] Specifically, shell dilatational elasticity E_s and viscosity κ_s modulate oscillation amplitude, damping, harmonic generation, and acoustic stability.[11–13] These viscoelastic characteristics of lipid-shelled MBs are strongly influenced by shell composition, including the type of lipid species and surfactants used.[14] Parameters such as lipid chain length,[15,16] degree of saturation,[15] and the incorporation of polyethylene glycol (PEG) moieties, along with their concentration dependent conformational regime (mushroom *versus* brush), have been shown to alter shell mechanics.[17–19] Additional components, such as cholesterol[20] or palmitic acid,[21] further modulate shell stiffness, packing density, and interfacial properties. Beyond viscoelasticity, shell composition also affects MB stability, gas diffusion rates, circulation half-life and acoustic durability.[22,23] Despite rigorous control over formulation and production protocols, previous studies have reported pronounced variability in the acoustic response of individual MBs, even within populations derived from the same batch.[24,25] In some instances, differences in viscosity or elasticity differed by orders of magnitude between individual MBs.[24,25] Consequently, such variability poses challenges for both high-resolution imaging applications and the optimization of ultrasound-mediated therapeutic strategies.

One currently debated explanation for this variability is heterogeneity within the lipid shell itself.[24,25] During MB formation, lipid mixtures can undergo phase separation, a phenomenon where lipid species with differing physicochemical properties unmix to form distinct microdomains.[24,26–30] These microdomains in lipid monolayers are commonly characterized through the framework of lipid phase states, typically studied at the gas–water interface using Langmuir–Blodgett films. Lipid organization is generally classified into four principal phase states, although intermediate or coexisting states may also occur. These include: a gaseous (G) phase, in which lipids exhibit minimal intermolecular interactions; a liquid-expanded (L_E) phase, characterized by increased lipid-lipid interactions while retaining high lateral mobility; a liquid-condensed (L_C) phase, in which lipids are densely packed and lateral mobility is substantially reduced; and a solid (S) phase, which is highly ordered with negligible lateral mobility.[31–33] The sizes, morphology, and spatial distribution of these domains depend on lipid composition,[26] chain length[16] and thermal history, including cooling rates during shell solidification.[29,30] Previous studies have shown that these microdomains can be reversibly altered by heating MBs above the lipid phase transition temperature followed by rapid cooling, suggesting a dynamic and metastable shell organization.[29,34] The presence of ordered and disordered lipid domains may influence multiple aspects of MB behavior. In addition to altering viscoelastic properties and acoustic scattering, it may affect gas dissolution rates, particularly through differences in permeability between ordered and disordered regions.[35] Furthermore, phase separation may influence PEG chain conformation and ligand distribution on the MB surface, with potential implications for circulation stability, targeting efficiency, and biological interactions.

Here we systematically investigate the formation and evolution of lipid microstructures within MB shells as well as to elucidate their role during periodic expansion and compression. We specifically examine whether these microstructures could account for the pronounced variability in acoustic scattering observed in previous studies.[24,25]

To address this, we introduce the 'cocktail method', an effective preparation strategy designed to homogenize the MB surface. We first benchmark these MBs against those produced *via* a standard protocol, evaluating their stability, yield, and size distribution. We then analyze the shell's component co-localization, solidification, and domain morphology. Finally, we investigate shell dynamics during expansion, measuring microviscosities *via* fluorescence lifetime imaging (FLIM), before assessing their viscoelastic properties through acoustic rheology and observing ultrasound-induced morphological changes. Finally, we suggest a mechanistic explanation, linking shell microstructure to differences in viscoelastic properties and to changes in MB behavior.

2. Experimental

2.1. Materials

1,2-Distearoyl-*sn-glycero*-3-phosphoethanol-amine-*N*-[poly(ethylene glycol)-5000] (DSPE-PEG5000), was purchased from Avanti. Distearoylphosphatidylcholine (DSPC) and DSPE-PEG-FITC were purchased from Broadpharm. Perfluorobutane (C_4F_{10}) was purchased from FluoroMed. Lipophilic tracers DiD and DiI were purchased from Lumiprobe. BODIPY-C-12 was purchased from MedChemExpress. Solvents were purchased from Merck. DSPE-PEG5000-sCy3 was synthesized in house from DSPE-PEG5000-NH2 (Broadpharm) and sCy3-NHS (Lumiprobe).

2.2. Preparation of liposomes

A lipid film was first produced by dissolving DSPC, and DSPE-PEG(5000) and/or modified lipids in different ratios dependent on the formulation in chloroform and subsequent solvent removal under reduced pressure using a rotary evaporator. The resulting lipid film was rehydrated with 10% glycerol in PBS (pH = 7,4) and stirred at 70 °C for 30 minutes. The warm lipid solution was sonicated for another 30 minutes in a bath sonicator yielding a polydisperse liposome solution. In case of fluorescently labeled MBs different percentages of membrane dyes DiI or DiD were added in DMSO (10 mg mL^{-1} stock concentration) to the warm liposome solution and sonicated for another 5 min. The liposomes were stored in the fridge for up to 2 weeks.

Standard formulation (87% DSPC, 8% DSPE-PEG5000, 5% DiI) was used unless noted otherwise.

2.3. Standard generation of MBs

The liposome solution was aliquoted into 4 mL septum vials (2 mL per vial; Infochroma AG) and heated to 70 °C for 30 minutes. Immediately post-heating, the vial headspace was replaced with perfluorobutane (C_4F_{10}), and the vials were

agitated for 45 seconds using a 3M CapMix device (4300 oscillations per min), then placed on ice for 10 minutes to produce polydisperse MBs. The resulting MBs were pooled into a 12 mL syringe and purified by differential centrifugation, three times at 100 g for 5 minutes.

2.4. Generation of MBs using the cocktail method

The liposome solution was aliquoted into 4 mL septum vials (2 mL per vial; Infochroma AG) and heated to 74 °C for 30 minutes. Immediately post-heating, the vial headspace was replaced with C_4F_{10}, and the vials were agitated for 45 seconds using a 3M CapMix device (4300 oscillations per min), then immediately poured into 15 mL of ice-cold PBS (pH =7.4) +10% glycerol under slow stirring (120 rpm) in an ice water bath. The resulting MBs were pooled into a 20 mL syringe and purified by differential centrifugation, three times at 100 g for 5 minutes.

2.5. Analysis of size, yield and stability

The size distribution, yield, and stability of the MBs were assessed using a Coulter counter Multisizer 4e (Beckman Coulter Life Sciences). For yield measurements, 2 μL of MB suspension was diluted in 10 mL of Isoton and analyzed with a 30 μm aperture tube.

For continuous stability measurements, all MB formulations were further diluted to a final concentration of 2.5×10^6 MBs mL^{-1} in Isoton. Measurements were recorded at 20-minute intervals. The area under the curve (AUC) of the size gated MB count was integrated between 1 and 8 μm to exclude disrupted MBs and lipid aggregates formed during decay. At each time point, the AUC_t was normalized to the initial area at t = 0 min (AUC_0) to calculate the relative stability as $\frac{AUC_t}{AUC_0}$ over time.

2.6. Lipid composition determination of the MBs with LC-MS analysis

Purified MBs were diluted in ultrapure water and destroyed in a sonicator bath. Each sample was analyzed by an LC-MS system (Agilent OpenLAB CDS 2.8) using selected ion monitoring (DiI-C18 at 833.6 m/z, DSPC at 790.6 m/z and DSPE-mPEG5k at 607.4 m/z). 1 μL sample was injected into an Agilent 1290 HPLC system equipped with a single quadrupole MSD over an Agilent Poroshell 120 EC-C8 column (1.9 μm 2.1 × 50 mm) heated at 40 °C. Three different eluents containing 0.2% formic acid were used. Eluent A: ultrapure water/acetonitrile 95 : 5, eluent B: acetonitrile and eluent C: methanol. The following eluent gradient was used: 0 min, A = 15% B = 35% C = 50%; 0–4 min, A = 15–0%, B = 35–5%; C = 50–95%; 4–5 min A = 0%, B = 5%; C = 95%; 5–6 min A = 0–15%, B = 5–35%; C = 95–50%.

2.7. Confocal imaging of shell structures and assessment of lipid dynamics

An inverted spinning disk confocal microscope (Nikon Eclipse Ti2 with Yokogawa CSU-W1 unit and Hamamatsu C13440-20CU Digital CMOS camera) equipped with a Plan apo λ 40× air objective, was used for all imaging experiments. MBs were mostly imaged between two coverslips separated by a stripe of double-sided tape that prevent squeezing of larger MBs, which reduces the occurrence of imaging artefacts. To study lipid structures and diffusion speeds, 10 second videos were taken with exposure times between 100 and 300 ms, allowing frame rates up to 10 FPS. ImageJ was used for adjustment of brightness and contrast as well as file conversion.

To investigate MB behavior under expansion and compression, a commercial μ-Slide I Luer chip (IBIDI; 1.5 Polymer, untreated; channel height 400 μm) was filled with a diluted MB suspension. One inlet of the chip was sealed with a valve, while the other was connected to a 20 mL syringe containing 10 mL MilliQ water and 3 mL of air. The syringe was mounted on a Standard PHD ULTRA™ CP syringe pump and oriented vertically with the syringe tip pointing downward. In this configuration, syringe withdrawal or infusion selectively expanded or compressed the gas phase above the liquid, thereby modulating the internal pressure of the system. A flow rate of 2 mL min^{-1} was applied, and videos were recorded for up to 2 min. Sequential expansion followed by compression was achieved using the withdraw/infusion mode (Videos S12 and S13).

MB surface dynamics were quantified through automated image analysis. Following the acquisition of confocal recordings at discrete timepoints, video sequences were processed *via* a custom Python script utilizing the OpenCV library.[36] In the initial processing stage, the MB was localized within the first frame by applying a Gaussian blur followed by a Hough Circle Transform (Fig. 1).[37] Detected candidates were discarded if they were of insufficient size or partially outside the frame boundaries. Upon selection of the candidate with the highest accumulator score, a binary mask was generated. To ensure the entire MB surface was encapsulated, the detected radius was expanded by 10%. Surface dynamics were quantified using Farneback's Optical Flow algorithm.[38] A three-level classical pyramid with a window size of 10 px was implemented; these parameters were selected to optimize the balance between noise rejection and sensitivity to local surface dynamics. The optical flow was calculated for the entire image and subsequently constrained by the binary bubble mask. For each frame, the spatial median of the optical flow magnitude was extracted, and these values were averaged across the duration of the video. Finally, displacement units were converted from pixels per frame to physical velocity (μm s^{-1}). It should be

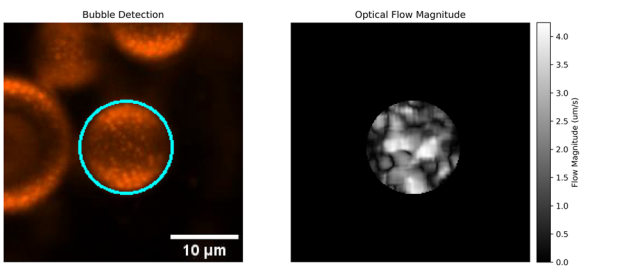

Fig. 1 Assessment of lipid diffusion kinetics during MB stabilization. Representative images of MB detection algorithm (left) and using Farneback's optical flow algorithm (right).

noted that only the velocity components projected onto the 2D imaging plane are captured. Furthermore, the analysis may be influenced by rotational or translational movement of the bubble as a whole, as well as the presence of floating debris. Despite these constraints, the method facilitates a robust quantitative comparison of surface dynamics over time.

2.8. Fluorescence lifetime imaging of MB surface

FLIM imaging was performed using a Leica TCS SP8 laser scanning confocal microscope including FLIM Falcon unit. Imaging was performed using a 63 × 1.4 NA Oil HC PL APO CS2 objective. Between 1000 and 3000 photons were collected per pixel, to assure accurate lifetime fitting. Images were analyzed using the software LAS-X STELLARIS8 SW and Leica Phasor analysis. Lifetimes were derived by fitting the obtained data with a monoexponential decay function. 2% of molecular rotor probe BODIPY-C-12 (10 mg mL^{-1} in DMSO) was added to the investigated MB formulations containing 90% DSPC and 10% DSPE-PEG5000 prior production.

2.9. Estimation of shell viscoelasticity from acoustically driven MB oscillations

Single MB dynamics was investigated using a custom-built vertical microscope for wide-field ultra-high-speed imaging.[25] This microscope is equipped with a water-dipping objective lens (Olympus LUMPLANFL 60×) and a tube lens (TL600-A, Thorlabs), providing a total magnification of 200×. Ultra-high-speed imaging was performed using a high-speed camera (HPV-X2, Shimadzu) at 10 million frames per second. Backlight illumination was provided by a laser (Cavilux Smart UHS, Cavitar, Tampere, FIN) with 80 μs light pulses. A water bath filled with deionized water at room temperature was used for ultrasound transmission. A custom-built test chamber with optically and acoustically transparent windows, which is immersed in the water bath, was used to confine the MBs. A broadband, focused ultrasound transducer (PA1612, Precision Acoustics; center frequency of 1.5 MHz, focal length of 85 mm, and beam width of approximately 4 mm at −6 dB) was positioned at a 45° angle in the water bath with respect to the test chamber.

To isolate a single MB, the test chamber was moved using a three-axis motorized microtranslation stage (PT3/M-Z8, Thorlabs) until a single MB was found with no other bubbles in the vicinity. The rule of thumb was to consider a bubble if there were no other bubbles present in the field of view (64 × 40 μm), ensuring a distance greater than 5–10 times the bubble radius. Then, the MB was acoustically driven using a 20-cycle sinusoidal pulse at 1.5 MHz with a peak negative pressure of 25 kPa.

Radius-time curves were extracted from the recordings using an image-processing algorithm. Unlike the previously reported protocol,[25] a correction of R_{corr} = 50 ± 30 nm was used for the bubble radius, considering the different light source used in the experimental setup. Illumination with the pulsed laser causes a Fresnel diffraction pattern around the MB, creating concentric rings that hinder accurate size measurement. Fluorescence microscopy avoids this issue because light emitted independently from the specimen on the MB shell prevents interference. We then evaluated the error by comparing the radius of the bubbles as measured by fluorescence and bright-field microscopy (data not shown). After correcting the bubble radius, resonance curves were obtained by evaluating the normalized maximum bubble radial expansion $\frac{R_{max}}{R_0} - 1$, with respect to the initial bubble radius R_0.

The viscoelastic properties of each tested MB were inferred using a grid search optimization algorithm to determine the theoretical radial time evolution of the bubble that results in minimum deviation between the empirical and theoretical maximum expansions of the bubble. We calculated the theoretical bubble response using the compressible Rayleigh–Plesset equation augmented by the Marmottant model[39] to account for the shell and the Zhou model[40] to accurately describe the gas core of the bubble.

The parameters used were initial surface tension σ = 0, ambient pressure p_0 = 102.2 kPa, water surface tension σ_w = 0.072 N m^{-1}, water dynamic viscosity μ = 0.000954 Pa s, water density ρ = 997.8 kg m^{-3}, specific heat ratio γ = 1.4, thermal conductivity K_s = 0.0259 W m^{-1} K^{-1}, specific gas constant R_g = 287 J kg^{-1} K^{-1}, gas temperature T_g = 295 K. The driving acoustic signal used in the simulations is the actual, experimentally recorded pressure pulse. A grid-search optimization approach was then applied over a predefined parameter space of E_s (0.1–0.6 N m^{-1}) and κ_s (5×10^{-9}–5×10^{-8} kg s^{-1}) values to minimize the discrepancy between experimentally measured and simulated bubble dynamics.

The asymmetry of radial oscillations was measured as the ratio EC between the relative expansion $E = \frac{R_{max}}{R_0} - 1$ and the relative compression $C = 1 - \frac{R_{min}}{R_0}$. A ratio $\frac{E}{C} < 0.5$ was classified as compression-only behavior while a ratio $0.5 \leq \frac{E}{C} \leq 2$ as normal oscillations.[41]

3. Results and discussion

3.1. Cocktail method in numbers

Previous studies[29,34] have shown that thermal treatment followed by rapid cooling can effectively melt lipid microdomains on MBs, resulting in a more homogeneous shell structure. However, this technique necessitates the use of pre-formed MBs, thereby introducing a post-processing step to an already labor-intensive fabrication protocol. In addition to extending production timelines, which is a critical constraint for MBs with limited shelf stability, thermal treatment may induce the partial expulsion of emulsifier lipids (*e.g.* DSPE-PEG5000) resulting in stoichiometric deviations from the intended shell composition and a reduction in total yield.[42]

To address these limitations, we developed the cocktail method, a protocol designed to thermally quench microdomain formation on MBs within the manufacturing process. This process prevents the crystallization of core lipid DSPC, yielding

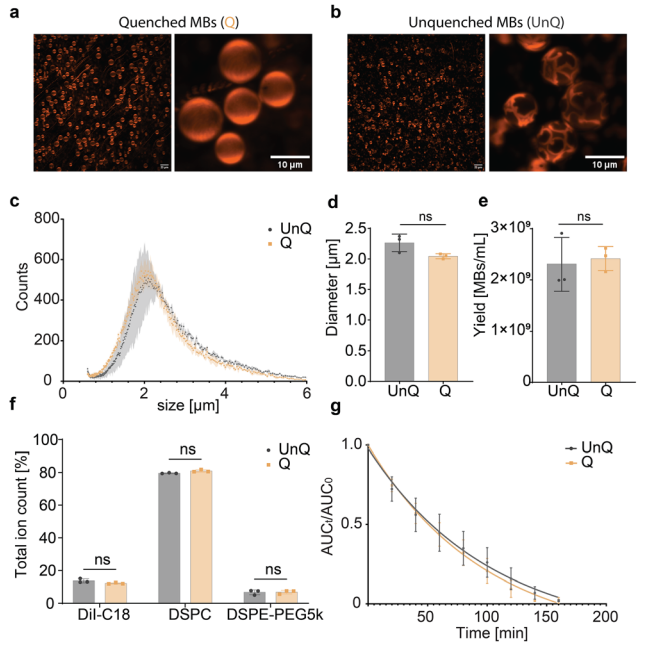

Fig. 2 Comparative characterization of the cocktail method (Q) *versus* standard MB fabrication protocol (UnQ). Representative confocal images of Q (a) and UnQ MBs (b). (c) Size distribution profiles of Q and UnQ samples after generation and differential centrifugation. (d) Quantitative comparison of the mean diameter. (e) Production yield comparison between the two methods. (f) Chemical composition analysis of Q and UnQ MBs determined *via* LC-MS. (g) Stability assessment of stirred MBs in Isoton over time, displayed as area under the curve (AUC) of the size distribution at $t = x$ divided by AUC at $t = 0$. Data are presented as mean ± SD of 3 individual MB batches.

in MBs with a more uniform lipid shell (Fig. 2a and b). MBs synthesized *via* the cocktail method and conventional passive cooling are hereafter referred to as quenched MBs (Q, Fig. 2a) and unquenched MBs (UnQ, Fig. 2b), respectively. Since lipid phase separation is thermally driven, occurring near the transition temperature of the core lipid (55 °C for DSPC), the liposome suspension is first heated above this temperature to ensure complete lipid dissolution. By maintaining this elevated temperature during shaking and immediately pouring the freshly formed MBs into an ice-cold buffer (instantaneous cooling from ~70 °C to 3 °C, Fig. S1), we prevent slow solidification that facilitates domain formation.

The cocktail method produces MBs with comparable size distribution (Fig. 2c and d) and yield (Fig. 2e) to those obtained using conventional cooling approaches (*e.g.*, passive cooling vial on ice). Unlike the cocktail method, standard passive cooling protocols are susceptible to lipid domain formation due to their slower thermal transition rates. Notably, LC-MS quantification of individual shell components, including the core lipid DSPC, emulsifier lipid DSPE-PEG5000, and membrane dye DiI, revealed no significant compositional differences between the two groups (Fig. 2f).

To assess the influence of shell morphology on MB stability, size distributions for both quenched and unquenched populations were monitored over time (Fig. 2g). MBs were diluted in Isoton and maintained under continuous stirring, with measurements recorded every 20 minutes. No significant difference in stability was observed between quenched and unquenched MBs, suggesting that enhanced shell homogeneity does not necessarily improve resistance to dissolution.

3.2. Co-localization of shell components

To examine the shell morphology and lipid phase states of quenched and unquenched MBs, we prepared a formulation consisting of fluorescently labeled emulsifier lipid DSPE-PEG5000-sCy3, the membrane dye DiD, emulsifier DSPE-PEG5000 and the core lipid DSPC in a molar ratio of 2 : 2 : 6 : 90, respectively. Hereby, the sCy3-labeled emulsifier maintains the native behavior of its unlabeled counterpart due to the negligible impact of the fluorophore attachment. Unlike the labeled emulsifier, DiD acts as an independent tracer that partitions based on local hydrophobicity rather than mimicking the specific molecular distribution of the individual shell components. The red-shifted dye DiD was utilized to ensure fluorescence orthogonality with DSPE-PEG-5000-sCy3. Due to its structural similarity and identical fatty acid chain length to DiI, DiD serves as a functionally equivalent probe with negligible impact on membrane dynamics.

Confocal fluorescence microscopy revealed a triphasic coexistence (Fig. 3a) within the shells of most unquenched MBs. This morphology consisted of a bi-phasic, solid-like structure characterized by a dye-excluded (non-fluorescent) core surrounded by a lateral concentration gradient of DiD. These domains were embedded within a third, viscous phase primarily composed of the emulsifier lipid DSPE-PEG5000-sCy3. In contrast, quenched MBs exhibited a homogeneous and smooth surface morphology, suggesting that rapid cooling effectively suppresses lateral phase separation (Fig. 3a and Fig. S2). Pearson's colocalization analysis indicated nearly complete colocalization of DiD and DSPE-PEG5000-sCy3 in the quenched MBs, whereas unquenched samples showed significantly lower spatial overlap (Fig. 3b).

According to classical thermodynamic definitions, phase separation should yield a discrete interfacial boundary between distinct phases. However, the observed monotonic increase in DiD intensity within the solid domains towards the edges

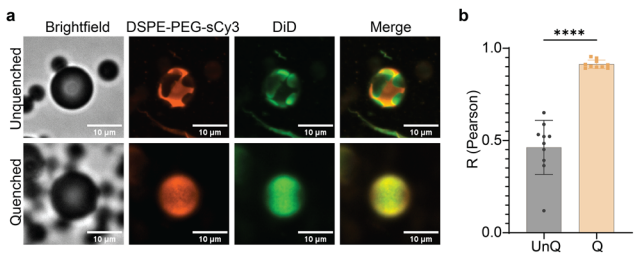

Fig. 3 Co-localization of individual shell components in Q and UnQ MBs (a) Representative images of unquenched (UnQ) and quenched (Q) MBs labeled with DSPE-PEG5000-sCy3 (orange) and DiD (green). (b) Pearson co-localization of DSPE-PEG5000sCy3 signal with membrane dye DiI. Data a represented as mean ± SD of ten individual MBs.

suggests that conventional phase terminology may be insufficient to describe this system. The observed behavior is more characteristic of a crystallization-nucleation-growth mechanism, wherein ordered DSPC domains originate at T_m = 55 °C. In such a mechanism, the domains continue growing until the temperature falls below a critical threshold, where the thermal fluctuations of individual lipids become insufficient to overcome the energy barriers required for crystalline lattice alignment. Consequently, the system enters a vitrified or glass-transition state, characterized by persistent intermolecular attractions within an amorphous solid or disordered precipitate with minimal molecular mobility.

In order to match these observations with previously described monolayer terminology, we consider the seemingly pure, crystalline DSPC domains as solid (S) phase, the glassy transition region at the domain edge, including DSPC and DiD as solid to liquid-condensed (S-L_C) phase and the remaining mobile phase, dominated by emulsifier lipid DSPE-PEG5000-sCy3 as liquid expanded (L_E) phase. This classification facilitates the interpretation of domain morphology despite the inability of fluorescence imaging to resolve the subtle transition between S and L_C phases, based on lipid mobility.

Notably, while earlier studies identified this three-phase coexistence as a minor sub-species, our results demonstrate it is, in fact, the predominant species under these experimental conditions.[29] This discrepancy may arise from differences in production methods, lipid compositions, the timing of imaging relative to MB stabilization, or a lower spatial resolution. To elucidate how the length and the resulting steric footprint of the emulsifier lipid influences lateral phase organization, we performed three-color co-localization using DiD and differently sized emulsifier lipids DSPE-PEG2000-FITC and DSPE-PEG5000-sCy3. Three-color co-localization analysis demonstrated that unquenched MBs comprise a heterogeneous mixture of three distinct phase-separated species, showing that even differently sized emulsifier lipids can unmix in unquenched MBs. In contrast, quenched MBs exhibited a uniform lipid distribution, indicative of a homogenous population (Fig. S3).

3.3. Shell solidification

To gain deeper insight into the formation dynamics of the MB lipid shell, we employed confocal fluorescence microscopy to monitor MBs at various stages after production, tracking individual MBs over time. Immediately after generation, the MB shell appeared highly fluid, with pronounced lateral lipid mobility, indicating a fully mobile membrane state. Domain formation was found to be temperature-dependent, while lipid diffusivity was strongly influenced by the available surface area (Fig. S4). During this phase, MBs adapted through gas exchange and diffusion-driven shrinking. As the MBs decreased in size, lipid mobility progressively slowed until the shell reached a solid-like state characterized by negligible lateral mobility (Fig. S5). Because continuous imaging of individual MBs proved challenging due to rapid and substantial changes in radius, in addition to formation of artefacts (*e.g.* dye precipitation) at the glass contact side, MBs of similar size were analyzed at different time points to reconstruct the chronological sequence of morphological transitions while maintaining consistent spatial resolution of surface features (Fig. 4). To investigate the long-term evolution of the lipid domain morphology, we performed additional imaging after 3 and 4 days, which confirmed the stability of the solidified states (Fig. S6 and S7).

To elucidate the roles of the individual lipid components, two formulations were investigated: one containing membrane dye DiI (Fig. 4a) and another incorporating the fluorescently labeled emulsifier lipid DSPE-PEG5000-sCy3 (Fig. 4b). To ensure signal orthogonality and prevent imaging artifacts, each membrane probe was imaged independently.

In unquenched DiI-labeled MBs, nucleation of the core lipid initiated almost immediately after production, coinciding with the temperature dropping below the phase transition threshold of the core lipid. Upon further cooling, the membrane dye DiI aggregated preferentially around these nascent core lipid crystals, while additional dye aggregates appeared randomly across the shell surface. These solidified lipid-dye domains, comprising two distinct phases, an inner S domain of pure DSPC as core crystal surrounded by an enriched S-L_C phase with increasing dye concentration towards the edges, remained embedded in a third, more fluid L_E phase that gradually decreased in mobility until visible lateral diffusion ceased completely. Incorporation of the fluorescent emulsifier lipid DSPE-PEG5000-sCy3 revealed that this component predominantly occupied the fluid L_E phase and did not form detectable aggregates or solid-like domains.

In contrast, quenched DiI-labeled MBs initially displayed heterogeneous aggregates that subsequently coalesced and annealed into a visually smooth and homogeneous surface as the shell solidified. Similarly, quenched DSPE-PEG5000-sCy3 MBs showed early-stage aggregate formation that evolved into a mesh-like structure enriched in labeled emulsifier lipid in the L_E phase, suggesting a higher local concentration of emulsifier between the solidified heterogenous lipid domains.

Collectively, these observations indicate that the MB shell undergoes a progressive transition from a fluid monolayer to a semi-solid composite structure. This structure consists of homogenous or heterogeneous lipid-dye islands (S or L_C states) embedded within a viscous matrix dominated by the emulsifier lipid (L_E state).

3.4. Shell dynamics and phase stability during expansion

After investigation of the phase states of individual components in the MB shell during formation, we investigated their behavior during slow volumetric expansion. Therefore, we built a custom pressure chamber composed of a syringe pump and a sealable 1-channel-IBIDI chip. This setup allowed for well-controlled pressure states, facilitating high-resolution observation of the expansion phase. During expansion of the unquenched DiI MBs, a separation of the solid domains (S) was clearly observed: the different sized core lipid islands and dye aggregates were preserved, with a dark, unlabeled phase in-between (Fig. 5a, UnQ, Video S5). Quenched DiI MBs exhibited a similar behavior, however separation resulted in more

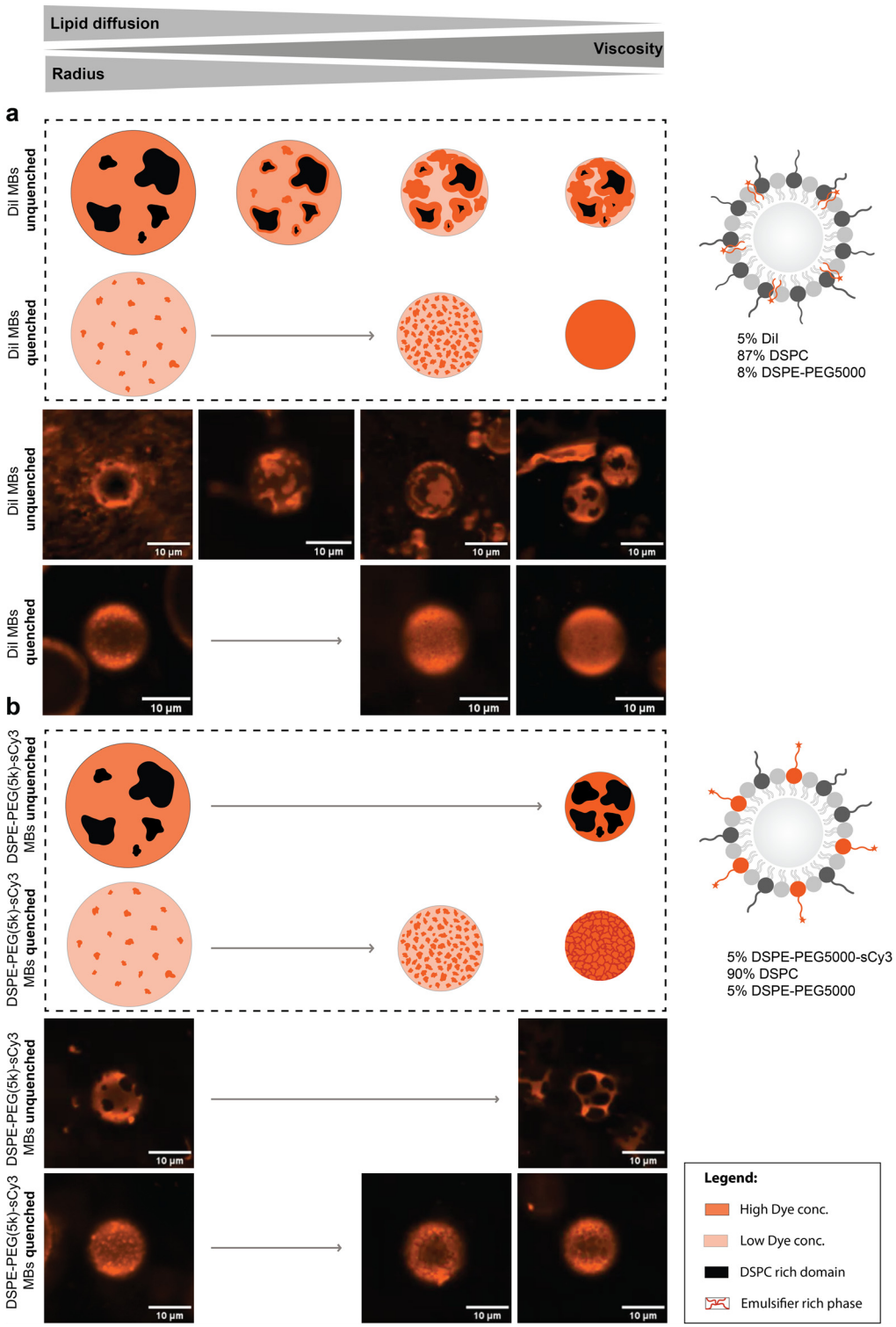

Fig. 4 Visualization of individual lipid components during MB shell solidification. Representative micrographs illustrate the morphological evolution of (a) DiI-labeled- unquenched (Video S1) and quenched (Video S2) and (b) DSPE-PEG5000-sCy3-labeled unquenched (Video S3) and quenched (Video S4) MBs during the stabilization process. Representative individual MBs were selected per column, supporting the illustrated schematic. The panels contrast the structural behavior of the lipid shell in quenched (Q) *versus* unquenched (UnQ) formulations over time.

uniformly sized heterogenous aggregates (Fig. 5a, Q, Video S6). In contrast, unquenched MBs with labeled emulsifier lipid DSPE-PEG5000-sCy3 displayed a markedly different trend. In these samples, the labeled emulsifier redistributed homogeneously between the islands during expansion (Fig. 5b, UnQ, Video S7). A similar trend was observed for the quenched MBs

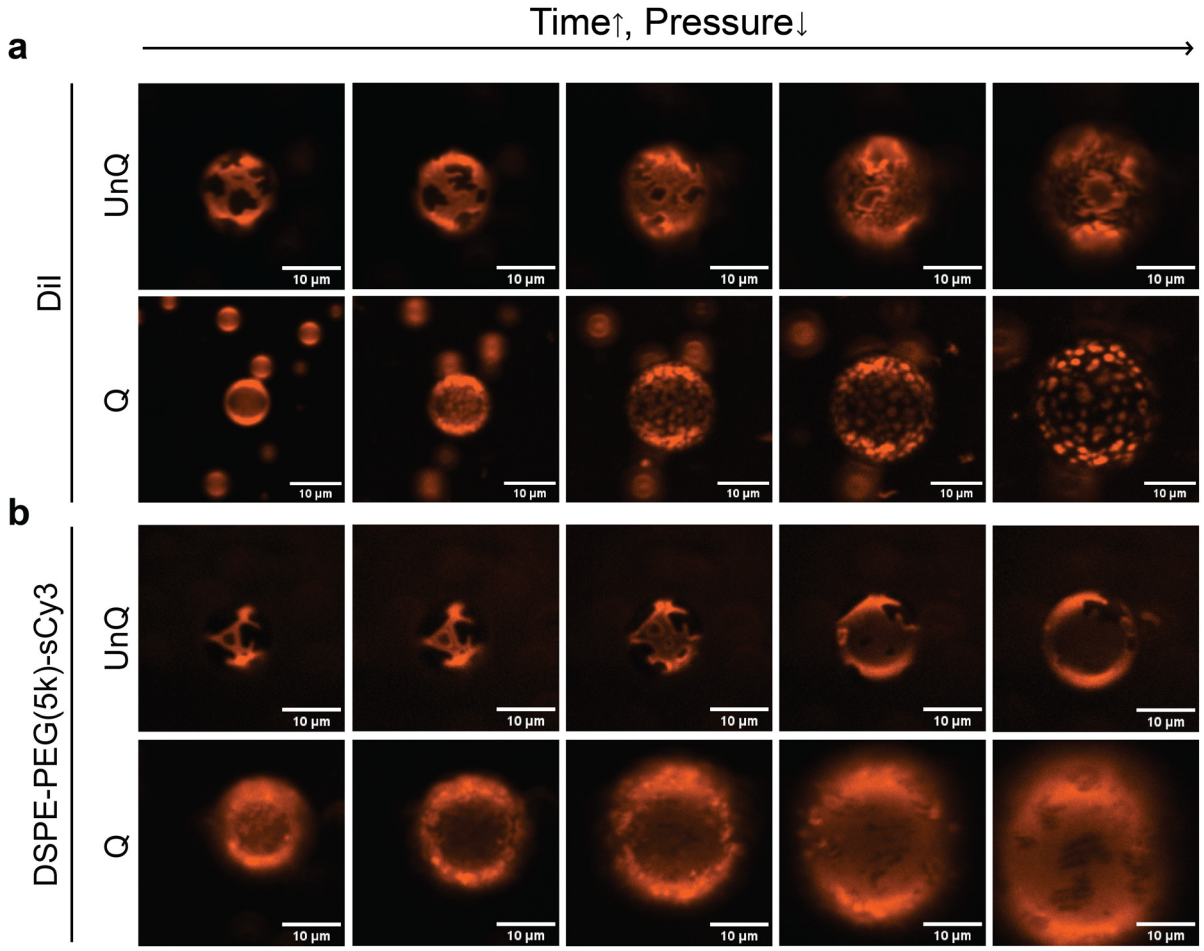

Fig. 5 Time-resolved imaging of MB shell expansion dynamics. Sequential frames extracted from video recordings illustrate the behavior of the lipid shell during volumetric expansion in either UnQ or Q (a) DiI-labeled MBs and (b) DSPE-PEG5000-sCy3-labeled MBs.

with the labeled emulsifier. During MB expansion, the emulsifier lipid dissolved and spread across the whole MB surface, while some solidified aggregates diffused through (Fig. 5b, Q and Video S8).

These findings suggest that the L_E phase primarily provides structural stability during expansion by covering the MBs surface, while core lipid and membrane dye remain in a more solidified state. Moreover, expansion of the quenched MBs suggests that even a homogeneously appearing surface likely contains at least two distinct lipid phases, most possibly reflecting the coexistence of similarly sized, heterogenous L_C domains within a viscous L_E phase. Although these slow-motion expansion timescales are orders of magnitude longer than an ultrasound pulse, the resistance to deformation of the solidified S domains or S-L_C precipitates suggests they remain intact during high-frequency oscillations. Consequently, the L_E phase likely has a stabilizing effect during a MB's volumetric oscillation.

3.5. Visualization of shell microviscosity

The localized lipid movement observed within the L_E regions during MB expansion suggests significant variations in viscoelasticity between distinct lipid phases. To investigate this hypothesis, we utilized the molecular rotor BODIPY C-12 (Fig. 6a), a fluorescent probe characterized by a viscosity-dependent lifetime, combined with FLIM. While BODIPY-C12 is traditionally employed to map viscosities in cellular environments,[43] derivatives have been successfully incorporated into MB formulations to estimate surface viscosity.[44] Previous studies, operating at a resolution of ~200 nm, identified lifetime variations both between individual MBs and across the surface of a single MB.[43] By using a Leica TCS SP8 laser scanning confocal microscope with higher sensitivity, we aimed to obtain a high-resolution qualitative overview of shell viscosity and directly correlate these variations with the lipid phases identified *via* confocal microscopy. In prior literature, probe lifetimes were calibrated using bulk methanol/glycerol mixtures.[43] However, while a linear correlation exists between lifetime and viscosity in bulk, translating 3D bulk measurements to viscosities in a 2D lipid monolayer at an interface can introduce significant scaling errors.[45] Consequently, we report lifetime differences as an indirect qualitative measure of viscosity, where higher lifetime indicates a higher local viscosity, hereafter described as microviscosity.

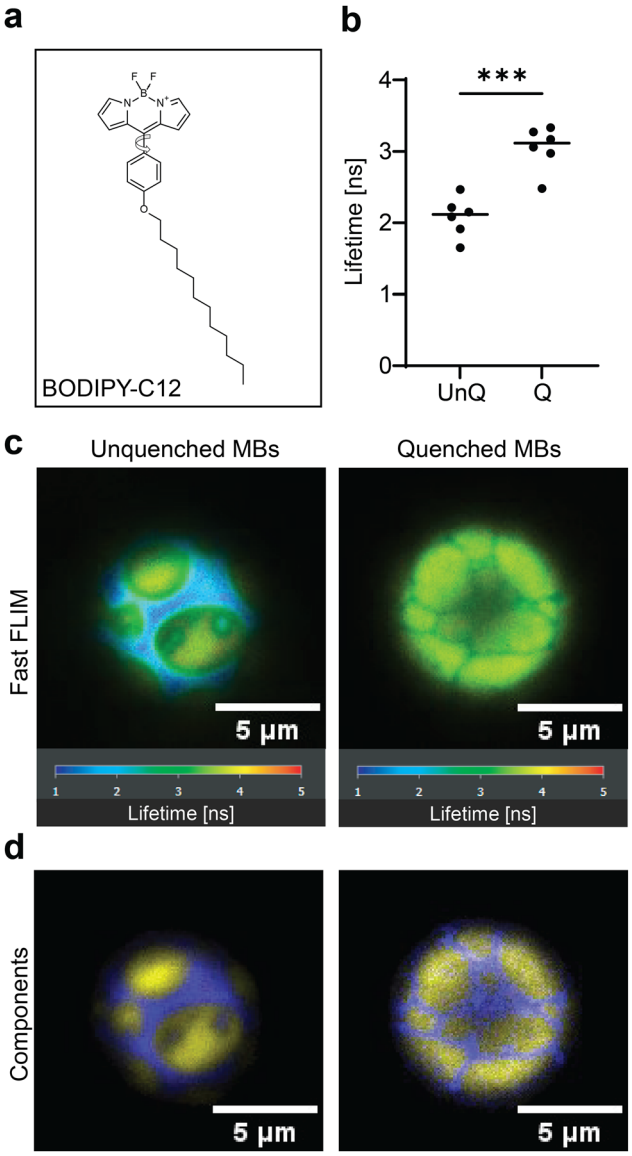

Fig. 6 Qualitative microviscosity mapping using molecular rotor probe combined with FLIM. (a) Chemical structure of molecular rotor probe BODIPY-C12. (b) Mean lifetime of BODIPY-C12 in UnQ *versus* Q MBs. A higher lifetime indicates a greater microviscosity (c) Representative unprocessed Fast FLIM images of an UnQ and a Q MB. (d) Representative images of lifetime-based unmixing into individual components, where multiple phases were defined and the detected lifetimes of the shortest (blue) and longest (yellow) are depicted.

By incorporating the rotor probe into both quenched and unquenched MBs, we mapped distinct lifetimes across both formulations (t_{UnQ} = 2,07 ± 0.25 ns, t_Q = 3.04 ± 0.28 ns), where the quenched population exhibited a higher mean lifetime, indicating a greater overall microviscosity (Fig. 6b–d). Supporting our confocal microscopy findings, FLIM revealed that each formulation comprises at least two phases, a high-viscosity phase likely S or L_C embedded within a lower-viscosity L_E matrix, however with a larger degree of unmixing in the unquenched MBs.

Due to the pronounced lipid unmixing in unquenched MBs, we could perform phase-specific lifetime mapping by defining ROIs and measuring the distinct lifetimes of the rotor probe (Fig. S8a–c). The S phase displayed an average lifetime twice as long as the L_E phase, signifying a substantial disparity in microviscosity (Fig. S8d). These results support the expansion video data, suggesting that the L_E phase, due to its fluidity, primarily accommodates volumetric changes during MB oscillation. A measurement of the individual phases in the quenched population was not possible because of the low degree of unmixing and fragmented size of the L_E phase.

Despite the significant differences in mean lifetimes between the phases, the phasor plot, which maps fluorescence decay kinetics into a 2-D frequency space, shows an uninterrupted lifetime trajectory suggesting a continuous viscosity gradient, peaking at the domain center and reaching a minimum within the L_E phase (Fig. S9). This gradual transition likely reflects the physical lipid crystallization process of the MB shell and additionally might also be an indicator for local lipid concentration ratios.

3.6. Estimation of shell viscoelasticity from acoustic response

The viscoelastic properties of the two distinct MB batches (unquenched and quenched) were characterized using an ultra-high-speed microscopy imaging system operating at 10 Mfps under ultrasound excitation, as previously described by Cattaneo and Supponen.[25] MBs were injected into the test chamber and allowed to adhere to the top window by flotation. A very low concentration was used to isolate them and minimize secondary Bjerknes forces upon acoustic excitation. A total of 201 unquenched MBs and 275 quenched MBs were insonified individually using a 20-cycle sinusoidal ultrasound pulse with a peak negative pressure of 25 kPa. This value was chosen instead of 40 kPa[25] to allow for detectable radial excursions while preventing shape deformation and related errors in measuring the equivalent radius through the bubble's cross-sectional area due to the loss of spherical symmetry. To estimate the shell rheological parameters, dilatational elasticity (E_s) and dilatational viscosity (κ_s), the experimental data were fitted to a nonlinear bubble dynamics model based on a modified Rayleigh–Plesset equation and the Marmottant shell model, as previously described.[25] The Marmottant model describes the dynamic properties of coated MBs by introducing an effective surface tension that depends on the instantaneous radius relative to the equilibrium radius. This effective surface tension defines three regimes. For radii below the buckling radius, the shell is buckled with a vanishing surface tension as the excess area is accommodated by folding. For radii between the buckling and rupture radii, the shell exhibits elastic behavior. The surface tension increases approximately linearly with expansion due to the finite elasticity of the shell. For radii exceeding the rupture radius, the shell fails, the interface behaves like that of a free bubble, and the surface tension is equal to that of the surrounding liquid.[39] The theoretical response of individual MBs is calculated by setting the initial surface tension σ_0 to zero, which assumes a buckling behavior

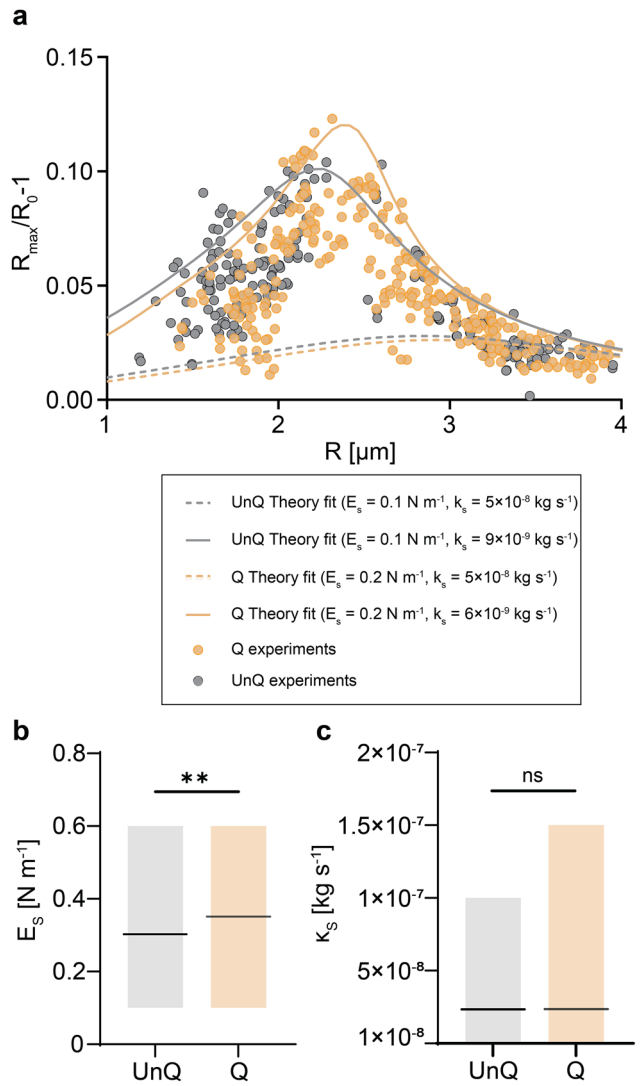

Fig. 7 Viscoelastic characterization of quenched (Q) and unquenched (UnQ) MBs. (a) Experimental normalized radial expansion of MBs under unquenched (gray dots) and quenched (orange dots) conditions. Overlaid are theoretical resonance curves derived from the bubble dynamics model; solid lines represent lower viscosity regimes, while dashed lines indicate higher viscosities. (b) Values for shell elasticity (E_S) and (c) shell viscosity (κ_S), with the box indicating the mean, minimum and maximum values of 201 MBs for the unquenched and 275 MBs for the quenched population.

of the shell for radii smaller than the equivalent radius. None of the MBs exhibited maximal radial expansion greater than the rupture radius, indicating that the elastic regime plays a main role in MB oscillation. Fig. 7a shows the distribution of the normalized maximum radial expansion across the range of equilibrium radii examined for unquenched (black dots) and quenched (orange dots) MBs. The data exhibit a peak at the resonance MB radius and demonstrate significant variability in the response of MBs of similar sizes.

Good overall agreement was obtained between the experimental data and theory with the following dilatational elasticity values: $E_{s(Q)}$ = 0.2 N m^{-1} and $E_{s(UnQ)}$ = 0.1 N m^{-1}. Theoretical curves were generated using upper-bound values, $\kappa_{s(Q)} = 5 \times 10^{-8}$ kg s^{-1} and $\kappa_{s(UnQ)} = 5 \times 10^{-8}$ kg s^{-1} (dashed lines), and lower-bound values, $\kappa_{s(Q)} = 6 \times 10^{-9}$ kg s^{-1} and $\kappa_{s(UnQ)} = 9 \times 10^{-9}$ kg s^{-1} (solid lines), thereby capturing most of the data points of the entire MB population (Fig. 7a). Considering the distribution of values obtained for the shell rheological parameters by fitting individual MB responses, the quenched MBs exhibited slightly higher mean dilatational elasticity ($E_{s(Q)}$ = 0.35 N m^{-1}) than the unquenched MBs ($E_{s(UnQ)}$ = 0.3 N m^{-1}), as well as more dispersed data toward higher values, as shown in Fig. 7b. These results suggest that quenched MBs are slightly stiffer than unquenched MBs. Conversely, the dilatational viscosity data distribution was nearly identical, with a mean value of $\kappa_s = 2 \times 10^{-8}$ kg s^{-1} (Fig. 7c).

Although there was good agreement between the experimental and theoretical responses for individual MBs, both the quenched and unquenched MB populations showed that neither population exhibited monoacoustic behavior for a fixed size, a topic that remains under investigation.

We then investigated nonlinear bubble oscillations by evaluating the ratio of the relative expansion $E = \frac{R_{max}}{R_0} - 1$ to the relative compression $C = 1 - \frac{R_{min}}{R_0}$. We defined the asymmetry of the bubble oscillation as compression-dominated when E/C < 0.5.[41]

Similar numbers of compression-only behavior were observed in both populations (136 out of 275 and 109 out of 201 for quenched and unquenched MBs, respectively, see Fig. S10), particularly around resonance (mean initial radius $R_{0(Q)} = 2.6 \times 10^{-6}$ m, $R_{0(UnQ)} = 2.4 \times 10^{-6}$ m).

Beyond the primary objective of characterizing the viscoelastic properties of quenched and unquenched MBs, we also noted a compelling side finding: a substantial difference in the number of surviving resonant bubbles recorded between the two populations. Because the ultrasound beamwidth at the focal point (~4 mm) is substantially larger than our field of view (64 × 40 μm), surrounding bubbles inevitably underwent repeated non-linear oscillations every time a target bubble was excited. Given that both populations possessed matching initial size distributions, the fact that we consistently captured a sufficient number of resonant-size bubbles for the quenched batches, but struggled to find them for the unquenched batches, suggests a higher stability around the resonance size for quenched MBs.

3.7. Acoustic stability

To evaluate acoustic stability, we quantified the decrease in MB radius following three consecutive insonication cycles. Both quenched and unquenched MBs exhibited comparable reductions in radius when close to resonance; however, a slight numerical trend (mean(UnQ) = 0.98; mean(Q) = 1.00) toward a greater radius reduction was observed for unquenched MBs, though this difference was not statistically significant (p = 0.18). (Fig. 8a and b). These findings suggest that acoustic stability

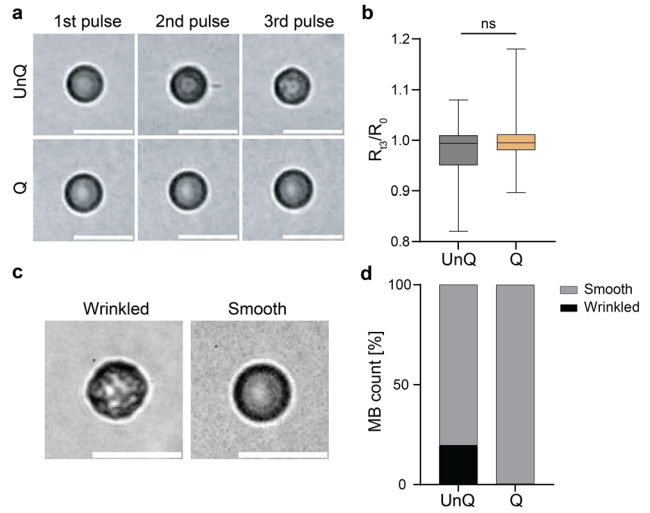

Fig. 8 Impact of acoustic stress on MB stability and surface structure. (a) Sequential monitoring of UnQ and Q MBs treated with repeated ultrasound pulses. (b) Assessment of shell stability measured by the mean reduction in radius after the 3rd pulse, displayed as Min/Max-boxplot (c) Representative examples of wrinkled and smooth shell morphologies. (d) Comparative analysis of surface morphology frequency in unquenched *versus* quenched samples. Scale bar = 10 μm.

may be affected by variations in lipid packing. However, more data is needed to confirm this relationship.

Moreover, qualitative differences emerged during high-frame-rate imaging performed for shell rheology analysis. Specifically, a subset of unquenched MBs displayed pronounced surface wrinkling during insonication (Fig. 8c and d). Such wrinkling events were rarely observed for quenched MBs, which mainly showed a smooth surface. A plausible explanation is the higher degree of shell homogeneity in quenched MBs. During compression-only oscillations, the L_E phase is preferentially shed in unquenched MBs, which enhances defect lines at the boundaries of S or L_C domains. As the shell becomes increasingly enriched in ordered phases, its ability to accommodate compressive strain through lateral reorganization decreases. Under repeated compression, the accumulated in-plane stress is therefore released preferentially through out-of-plane deformation along these defect lines. This mechanism promotes localized wrinkling and buckling of the shell, producing the irregular morphologies frequently observed in unquenched MBs.

4. Conclusion

In this study, multi-modal observations of individual MB shell components suggest that the cause for domain formation on lipid shelled MBs is a stepwise crystallization and precipitation behavior rather than a phase separation. Although thermally quenched MBs appear macroscopically homogeneous when visualized solely with DiI, the use of the labeled emulsifier DSPE-PEG5000sCy3 reveals a predominant accumulation of emulsifier between heterogeneous lipid precipitates. This indicates the coexistence of rigid patches alongside a viscous L_E phase dominated by emulsifier, which might be assigned to the mismatch in physicochemical properties of the individual lipid species.

Fluorescence imaging of MBs during radial expansion provided direct mechanical evidence for a phase-dependent behavior: rigid S or L_C domains remain largely unchanged in size, whereas the L_E phase redistributes homogeneously between solidified domains. These observations are likely driven by the substantial differences in viscoelasticity, which could be visualized using the viscosity dependent molecular rotor probe BODIPY-C12 in combination with FLIM imaging.

Complementing these structural observations, acoustic rheological measures revealed that quenched MBs possess a slightly higher elasticity. However, the largely comparable variability in shell viscosity and the marginal differences in elasticity suggest that lipid organization alone is an insufficient explanation for the observed scatter in the viscoelastic properties. Therefore, neither unquenched nor quenched MBs can be considered monoacoustic. Critically, LC-MS analysis showed no significant compositional differences between quenched and unquenched MB populations, implying that the observed variations in mechanical properties (E_s, κ_s) can arise from differences in lipid packing density and phase organization. However, we regularly observed lipid shedding almost exclusively in L_E regions, during the stabilization process (Fig. S11 and Video S9) as well as during compression experiments (Fig. S12 and Videos S10 and S11). This localized material loss likely induces progressive compositional shifts and might contribute to the in-batch variability and could also explain the observed shell stiffening after repeated insonication.[13]

A single-phase lipid shell might offer greater buckling resistance, higher stability and more uniform acoustic behavior; however, the physicochemical differences of the used lipids (DSPC, DSPE-PEG5000) might inevitably result in a certain degree of phase separation and inhomogeneity of the shell. While combining thermal quenching with microfluidic production might offer a promising route towards shell uniformity, achieving a truly homogeneous shell may ultimately necessitate a change in lipid composition. By shedding more light on shell structure and lipid composition, this study supports the rational design of microbubbles with more predictable acoustic behaviors, ultimately enhancing their efficacy in targeted medical diagnostics and therapies.

Author contributions

PP: conceptualization, methodology, investigation, analysis visualization, writing, review & editing. GG: methodology, investigation, analysis, writing, review & editing. JB: methodology, investigation, analysis, review & editing. TG: methodology, investigation, analysis, review & editing. MC: methodology, analysis, review & editing. GCL: methodology, review & editing. NB: review & editing. IO: review & editing. JK: methodology. OS: conceptualization, resources, review & editing. SS: project administration,

funding acquisition, conceptualization, resources, writing, review & editing.

Conflicts of interest

There are no conflicts to declare.

Data availability

The data supporting the findings of this study have been deposited in the ETH research collection and can be accessed at: https://doi.org/10.3929/ethz-c-000797950.

Supplementary information (SI) containing supporting figures. See DOI: https://doi.org/10.1039/d6sm00286b.

Acknowledgements

This study was funded by the Strategic Focal Area ''Personalized Health and Related Technologies'' of the ETH Domain, grant number 2022-580, and by the Swiss National Science Foundation, grant number 205321_204789. The authors would also like to thank Edina Gashi, for the synthesis of the labeled emulsifier and the staff at the ETHZ imaging core facility ScopeM for technical support, particularly Dr. Dorothea Pintosi. During the preparation of this work the authors used Gemini 3.1 Pro to improve the readability and language of some portions of the manuscript. After using this tool, the authors reviewed and edited the content as needed and take full responsibility for the content of the published article.

References

1 P. Frinking, T. Segers, Y. Luan and F. Tranquart, *Ultrasound Med. Biol.*, 2020, **46**, 892–908.
2 M. Siepmann, G. Schmitz, J. Bzyl, M. Palmowski and F. Kiessling, *IEEE Int. Ultrason. Symp.*, 2011, 1906–1908.
3 O. Couture, B. Besson, G. Montaldo, M. Fink and M. Tanter, *IEEE Int. Ultrason. Symp.*, 2011, 1285–1287.
4 A. F. L. Schinkel, M. Kaspar and D. Staub, *Int. J. Cardiovasc. Imaging.*, 2015, **32**, 35–48.
5 M. Overvelde, V. Garbin, J. Sijl, B. Dollet, N. de Jong, D. Lohse and M. Versluis, *Ultrasound Med. Biol.*, 2010, **36**, 2080–2092.
6 A. J. Sojahrood, H. Haghi, T. M. Porter, R. Karshafian and M. C. Kolios, *Phys. Fluids*, 2021, **33**(7), DOI: 10.1063/5.0051463/1058879.
7 T. van Rooij, Y. Luan, G. Renaud, A. F. W. van der Steen, M. Versluis, N. de Jong and K. Kooiman, *Ultrasound Med. Biol.*, 2015, **41**, 1432–1445.
8 M. Cattaneo, G. Guerriero, G. Shakya, L. A. Krattiger, L. G. Paganella, M. L. Narciso and O. Supponen, *Nat. Phys.*, 2025, **21**, 590–598.
9 S. Hernot and A. L. Klibanov, *Adv. Drug Delivery Rev.*, 2008, **60**, 1153–1166.
10 T. Segers, E. Gaud, M. Versluis and P. Frinking, *J. Acoust. Soc. Am.*, 2018, **144**, 1852.
11 N. De Jong, A. Bouakaz and P. Frinking, *Echocardiography*, 2002, **19**, 229–240.
12 M. A. Parrales, J. M. Fernandez, M. Perez-Saborid, J. A. Kopechek and T. M. Porter, *J. Acoust. Soc. Am.*, 2014, **136**, 1077–1084.
13 T. Segers, L. De Rond, N. De Jong, M. Borden and M. Versluis, *Langmuir*, 2016, **32**, 3937–3944.
14 S. Dicker, M. Mleczko, M. Siepmann, N. Wallace, Y. Sunny, C. R. Bawiec, G. Schmitz, P. Lewin and S. P. Wrenn, *Ultrasound Med. Biol.*, 2013, **39**, 1292–1302.
15 S. Garg, A. A. Thomas and M. A. Borden, *Biomaterials*, 2013, **34**, 6862.
16 M. A. Borden and M. L. Longo, *Langmuir*, 2002, **18**, 9225–9233.
17 H. Zhang, C. Lu, A. C. H. Yu and P. Qin, *Acta Biomater.*, 2025, **204**, 596–609.
18 R. H. Azami, M. Aliabouzar, J. Osborn, K. N. Kumar, F. Forsberg, J. R. Eisenbrey, S. Mallik and K. Sarkar, *Ultrasound Med. Biol.*, 2022, **48**, 1720–1732.
19 J. A. Navarro-Becerra, J. I. Castillo and M. A. Borden, *ACS Biomater. Sci. Eng.*, 2024, **10**, 3331–3342.
20 S. A. G. Langeveld, I. Beekers, G. Collado-Lara, A. F. W. van der Steen, N. de Jong and K. Kooiman, *Pharmaceutics*, 2021, **13**, 119.
21 B. van Elburg, K. Bruil, G. Lajoinie, M. Borden, M. Versluis and T. Segers, *Langmuir*, 2025, **41**, 28313–28321.
22 J. J. Kwan and M. A. Borden, *Adv. Colloid Interface Sci.*, 2012, **183–184**, 82–99.
23 M. M. Lozano and M. L. Longo, *Langmuir*, 2009, **25**, 3705–3712.
24 S. Spiekhout, B. van Elburg, J. Voorneveld, N. de Jong, M. Versluis, J. G. Bosch and T. Segers, *Appl. Phys. Lett.*, 2024, **124**(23), DOI: 10.1063/5.0215736/3295952.
25 M. Cattaneo and O. Supponen, *Soft Matter*, 2023, **19**, 5925–5941.
26 S. A. G. Langeveld, I. Beekers, G. Collado-Lara, A. F. W. van der Steen, N. de Jong and K. Kooiman, *Pharmaceutics*, 2021, **13**, 119.
27 M. Borden, *Soft Matter*, 2009, **5**, 716–720.
28 M. A. Borden, D. E. Kruse, C. F. Caskey, S. Zhao, P. A. Dayton and K. W. Ferrara, *IEEE Trans. Ultrason. Ferroelectr. Freq. Control*, 2005, **52**, 1992–2002.
29 M. A. Borden, G. V. Martinez, J. Ricker, N. Tsvetkova, M. Longo, R. J. Gillies, P. A. Dayton and K. W. Ferrara, *Langmuir*, 2006, **22**, 4291–4297.
30 M. A. Borden, G. Pu, G. J. Runner and M. L. Longo, *Colloids Surf., B*, 2004, **35**, 209–223.
31 C. M. Knobler and R. C. Desai, *Annu. Rev. Phys. Chem.*, 1992, **43**, 207–236.
32 F. O. De Oliveira and M. N. Tamashiro, *Langmuir*, 2019, **35**, 3848–3858.
33 K. Y. C. Lee, *Annu. Rev. Phys. Chem.*, 2008, **59**, 771–791.
34 M. J. Benchimol, M. J. Hsu, C. E. Schutt, D. J. Hall, R. F. Mattrey and S. C. Esener, *Soft Matter*, 2013, **9**, 2384–2388.
35 G. Pu, M. L. Longo and M. A. Borden, *J. Am. Chem. Soc.*, 2005, **127**, 6524–6525.

36 G. Bradski, *Dr. Dobb's J.*, 2000, **25**, 120–123.
37 R. O. Duda and P. E. Hart, *Commun. ACM*, 1972, **15**, 11–15.
38 G. Farnebäck, in *Image Analysis*, ed J. Bigun and T. Gustavsson, Springer Berlin Heidelberg, Berlin, Heidelberg, 2003, pp. 363–370.
39 P. Marmottant, S. van der Meer, M. Emmer, M. Versluis, N. de Jong, S. Hilgenfeldt and D. Lohse, *J. Acoust. Soc. Am.*, 2005, **118**, 3499–3505.
40 G. Zhou, *J. Acoust. Soc. Am.*, 2021, **149**, 923–933.
41 T. Van Rooij, I. Beekers, K. R. Lattwein, A. F. W. Van Der Steen, N. De Jong and K. Kooiman, *IEEE Trans. Ultrason. Ferroelectr. Freq. Control*, 2017, **64**, 785–797.
42 B. van Elburg, A. Lassus, S. Cherkaoui, G. Lajoinie, M. Versluis and T. Segers, *J. Colloid Interface Sci.*, 2025, **685**, 449–457.
43 M. K. Kuimova, G. Yahioglu, J. A. Levitt and K. Suhling, *J. Am. Chem. Soc.*, 2008, **130**, 6672–6673.
44 N. A. Hosny, G. Mohamedi, P. Rademeyer, J. Owen, Y. Wu, M. X. Tang, R. J. Eckersley, E. Stride and M. K. Kuimova, *Proc. Natl. Acad. Sci. U. S. A.*, 2013, **110**, 9225–9230.
45 N. O. Jaensson, P. D. Anderson and J. Vermant, *J. Nonnewton. Fluid Mech.*, 2021, **290**, 104507.